



Predictive Cost Adaptive Control of Shock-Boundary-Layer Interaction in a Scramjet Inlet

Jacob C. Vander Schaaf*
University of Michigan, Ann Arbor, Michigan, 48109

Ragini Acharya†
University of Tennessee Space Institute, Tullahoma, Tennessee, 37388

Dennis S. Bernstein‡
University of Michigan, Ann Arbor, Michigan, 48109

The present paper investigates the feasibility of adaptive feedback control for controlling shock-boundary-layer interaction (SBLI) physics by modulating the thickness of the boundary layer. The approach taken in this paper is predictive cost adaptive control (PCAC). PCAC uses recursive least squares (RLS) with variable-rate forgetting for online, closed-loop system identification. At each time step, RLS-based system identification updates the coefficients of an input-output model whose order is specified by the user. To determine control inputs, PCAC uses quadratic programming for receding-horizon optimization, which enforces magnitude- and rate-saturation constraints on the control input as well as constraints on measured outputs. To enable output-feedback control, PCAC uses the block-observable canonical form realization, which provides exact state estimation at each step. PCAC can be used with a reference model, and unknown disturbances may be either matched or unmatched. During operation, PCAC uses sampled pressure data and requests a bleed mass-flow rate. Other than specifying the model order, optimization horizon, and forgetting parameters, PCAC operates under cold-start conditions without the need for any prior control-oriented model. Closed-loop simulations consider a pressure command specified at the location of a pressure sensor situated near the wall and bleed port, whose mass-flow rate is specified by PCAC. Numerical examples demonstrate the ability to control the pressure at the sensor location and thus the means for modifying the SBLI and boundary-layer thickness.

I. Introduction

The complex flow field in a scramjet flowpath has been the subject of intense interest and study for several decades [1–5]. Many features of the flow field also occur in supersonic wind tunnel nozzles and diffusers. Shock-boundary-layer interaction (SBLI) is a major contributor to the formation of the pseudo-shock train in the scramjet flowpath, especially the inlet and isolator. This interaction can also be seen at the start of the shock train in Figure 1.

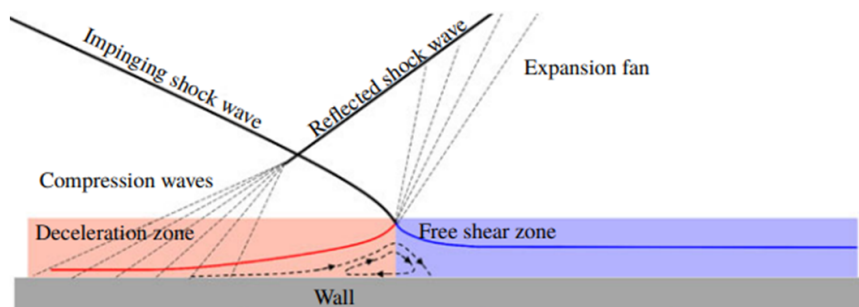


Fig. 1 Schematic of shock wave boundary-layer interaction [6]

*Ph.D. Candidate, Department of Aerospace Engineering, jacobcvs@umich.edu.

†Associate Professor, Aerospace Engineering, AIAA Associate Fellow, ragini.acharya@utsi.edu.

‡Professor, Department of Aerospace Engineering, dsbaero@umich.edu.

Impingement of a shock wave on the boundary layer increases the static pressure in the boundary layer, resulting in an adverse pressure gradient. A strong adverse pressure gradient can result in reverse flow near the surface if the boundary layer is thick, resulting in a phenomenon known as boundary-layer separation. Flow reversal and separation in the boundary layer initiates a nonlinear progression of events, including increased turbulence production, generation of expansion fans, and loss of total pressure due to the separation, resulting in detrimental effects on scramjet efficiency and operability.

Because of these undesirable effects, controlling the negative consequences of SBLI to prevent flow separation in the boundary layer has many benefits. There are several methods for controlling SBLI including boundary-layer suction, also known as bleed. Boundary-layer suction attempts to reduce the boundary layer thickness so that it can sustain an adverse pressure gradient due to shock impingement on the boundary layer. Boundary-layer suction has been shown by Sethuraman et al. [7] to reduce shock-train oscillations and the length of the shock train. Boundary-layer suction is the process of removing fluid near the wall where the boundary layer is formed. This method is used in the present paper to mitigate the increase of boundary-layer thickness due to shock-wave impingement on the turbulent boundary layer, thereby stabilizing the boundary layer and preventing flow separation near the foot of the shock as well as the ensuing total pressure loss and potential loss of scramjet operation.

Numerous studies have focused on determining the physical implementation of boundary-layer suction, including rectangular suction slots located on the spanwise length and side-walls of the scramjet flowpath. Research has focused on assessing the bleed-mass flow rate as well as the size of the bleed slots to ensure that flow is not choked in the bleed slots. Considering that these physical quantities depend on local Mach number, total pressure, and total temperature near the slot, it is difficult to find a universally applicable value for the bleed-mass flow rate. This significant challenge has been addressed in the present research by coupling an adaptive control algorithm with the SBLI physics so that the bleed-mass flow rate can be determined during operation rather than as a pre-determined value.

The present paper investigates the feasibility of using feedback control to influence the SBLI physics by controlling the thickness of the boundary layer. The technical approach utilized in this paper is based on predictive cost adaptive control (PCAC). As an indirect adaptive control extension of model predictive control (MPC), PCAC uses recursive least squares (RLS) with variable-rate forgetting (VRF) for online, closed-loop system identification [8–12]. At each time step, RLS-based system identification updates the coefficients of an input-output model whose order is specified by the user. To determine control inputs, PCAC uses quadratic programming for receding-horizon optimization, which enforces magnitude- and rate-saturation constraints on the control input as well as constraints on measured outputs. To enable output-feedback control, PCAC uses the block-observable canonical form (BOCF) realization, which provides exact state estimation at each step [13].

PCAC can be used with a reference model, and unknown disturbances may be either matched or unmatched. During operation, PCAC uses sampled pressure data and requests bleed mass-flow rate. Other than specifying the model order, optimization horizon, and forgetting parameters, PCAC operates under cold-start conditions without the need for any prior control-oriented model.

Detailed flowfield simulations were performed in the Viscous Upwind aLgorithm for Complex flow ANalysis Navier-Stokes code (VULCAN) [14], which is a Navier-Stokes flow solver for structured and unstructured cell-centered, multi-block grids. A structured multi-block grid system has been utilized with Reynolds-Averaged Navier-Stokes (RANS), which utilized PDE-based turbulence models. A robust upwind-biased algorithm was used for the Reynolds-averaged simulations, and a low-dissipation numerical framework has been used for the simulations.

The closed-loop VULCAN simulations consider a pressure command specified at the location of a pressure sensor situated near the wall and bleed port, whose mass-flow rate is specified by PCAC. The numerical examples demonstrate the ability to control the pressure at the sensor location and thus the means for modifying the SBLI and boundary-layer thickness.

II. Review of Predictive Cost Adaptive Control

As shown in Figure 2, predictive cost adaptive control (PCAC) combines online identification with output-feedback model predictive control (MPC). PCAC uses no a priori modeling information aside from a suitable model order for system identification, nor does it use probing signals.

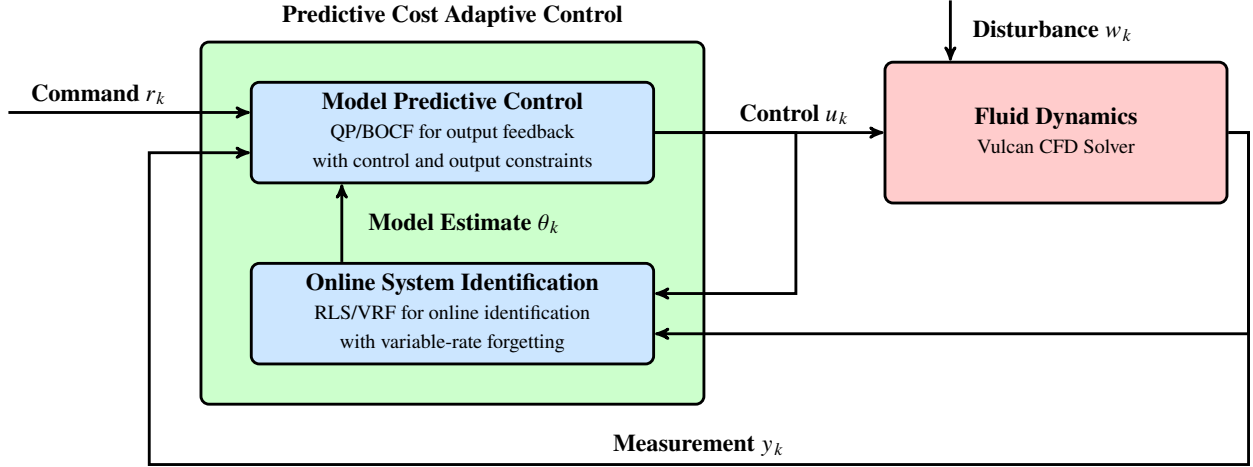


Fig. 2 PCAC block diagram. The online, closed-loop system identification is based on recursive least squares (RLS) with variable-rate forgetting (VRF). The quadratic programming algorithm uses the updated model parameters θ_k to specify the control input u_k .

A. Online Identification

To perform online identification, we first consider the MIMO input-output model

$$\hat{y}_k = - \sum_{i=1}^{\hat{n}} \hat{F}_i y_{k-i} + \sum_{i=1}^{\hat{n}} \hat{G}_i u_{k-i}, \quad (1)$$

where $k \geq 0$ is the step, $\hat{n} \geq 1$ is the identification data window, $\hat{F}_i \in \mathbb{R}^{p \times p}$ and $\hat{G}_i \in \mathbb{R}^{p \times m}$ are the estimated model coefficients, and $u_k \in \mathbb{R}^m$, $y_k \in \mathbb{R}^p$, and $\hat{y}_k \in \mathbb{R}^p$ are the inputs, outputs, and predicted outputs. We estimate \hat{F}_k and \hat{G}_k online using recursive least squares with variable-rate forgetting (RLS/VRF), by minimizing the cost function [9]

$$J_k(\hat{\theta}) = \sum_{i=0}^k \frac{\rho_i}{\rho_k} z_i^T(\hat{\theta}) z_i(\hat{\theta}) + \frac{1}{\rho_k} (\hat{\theta} - \theta_0)^T P_0^{-1} (\hat{\theta} - \theta_0), \quad (2)$$

where $\rho_k \triangleq \prod_{j=0}^k \lambda_j^{-1} \in \mathbb{R}$, $\lambda_k \in (0, 1]$ is the forgetting factor, $P_0 \in \mathbb{R}^{[\hat{n}p(m+p)] \times [\hat{n}p(m+p)]}$ is positive definite, $\theta_0 \in \mathbb{R}^{[\hat{n}p(m+p)]}$ is the initial estimate of the coefficient vector, and the performance variable $z_i(\hat{\theta}) \in \mathbb{R}^p$ is defined as

$$z_k(\hat{\theta}) = y_k - \phi_k \hat{\theta}. \quad (3)$$

The vector $\hat{\theta} \in \mathbb{R}^{[\hat{n}p(m+p)]}$ of coefficients to be estimated is

$$\hat{\theta} \triangleq \text{vec} \begin{bmatrix} \hat{F}_1 & \cdots & \hat{F}_{\hat{n}} & \hat{G}_1 & \cdots & \hat{G}_{\hat{n}} \end{bmatrix} = \text{vec} \begin{bmatrix} \hat{\theta}_{\hat{F}} & \hat{\theta}_{\hat{G}} \end{bmatrix},$$

where $\hat{\theta}_{\hat{F}}$ and $\hat{\theta}_{\hat{G}}$ are the estimates of the denominator and numerator coefficients, defined by

$$\hat{\theta}_{\hat{F}} \triangleq \text{vec} \begin{bmatrix} \hat{F}_1 & \cdots & \hat{F}_{\hat{n}} \end{bmatrix}, \quad (4)$$

$$\hat{\theta}_{\hat{G}} \triangleq \text{vec} \begin{bmatrix} \hat{G}_1 & \cdots & \hat{G}_{\hat{n}} \end{bmatrix}. \quad (5)$$

With the regressor matrix $\phi_k \in \mathbb{R}^{p \times [\hat{n}p(m+p)]}$ defined by

$$\phi_k \triangleq \begin{bmatrix} -y_{k-1}^T & \cdots & -y_{k-\hat{n}}^T & u_{k-1}^T & \cdots & u_{k-\hat{n}}^T \end{bmatrix} \otimes I_p,$$

the global minimizer $\theta_{k+1} \triangleq \operatorname{argmin}_{\hat{\theta}} J_k(\hat{\theta})$ of (2) is

$$L_k = \lambda_k^{-1} P_k, \quad (6)$$

$$P_{k+1} = L_k - L_k \phi_k^T (I_p + \phi_k L_k \phi_k^T)^{-1} \phi_k L_k, \quad (7)$$

$$\theta_{k+1} = \theta_k + P_{k+1} \phi_k^T (y_k - \phi_k \theta_k). \quad (8)$$

The variable-rate forgetting factor λ_k is given by [12]

$$\lambda_k = \frac{1}{1 + \eta g(z_{k-\tau_d}, \dots, z_k) \mathbf{1}[g(z_{k-\tau_d}, \dots, z_k)]}, \quad (9)$$

where $\mathbf{1}: \mathbb{R} \rightarrow \{0, 1\}$ is the unit step function, and

$$g(z_{k-\tau_d}, \dots, z_k) \triangleq \sqrt{\frac{\tau_n (\Sigma_{\tau_n}(z_{k-\tau_n}, \dots, z_k) \Sigma_{\tau_d}(z_{k-\tau_d}, \dots, z_k)^{-1})}{\tau_d c}} - \sqrt{f},$$

where $\eta > 0$ and $p \leq \tau_n < \tau_d$ represent numerator and denominator window lengths. Σ_{τ_n} and Σ_{τ_d} are the sample variances of the respective window lengths, and the threshold constant f is described in [15, 16]. The constant c , based on the windows lengths is described in [15]. The estimator coefficients $\hat{\theta}$ can be written in the block observable canonical form with matrices \hat{A}_k , \hat{B}_k , and \hat{C}_k given by

$$\hat{A}_k \triangleq \begin{bmatrix} -\hat{F}_{1,k} & I_p & \cdots & \cdots & 0_{p \times p} \\ \vdots & 0_{p \times p} & \ddots & & \vdots \\ \vdots & \vdots & \ddots & \ddots & 0_{p \times p} \\ \vdots & \vdots & & \ddots & I_p \\ -\hat{F}_{\hat{n},k} & 0_{p \times p} & \cdots & \cdots & 0_{p \times p} \end{bmatrix}, \quad \hat{B}_k \triangleq \begin{bmatrix} \hat{G}_{1,k} \\ \hat{G}_{2,k} \\ \vdots \\ \hat{G}_{\hat{n},k} \end{bmatrix}, \quad (10)$$

$$\hat{C}_k \triangleq \begin{bmatrix} I_p & 0_{p \times p} & \cdots & 0_{p \times p} \end{bmatrix}. \quad (11)$$

B. Model Predictive Control

Model predictive control (MPC) uses a model of the system to optimize its performance over a future finite interval of time. The optimization yields a sequence of controls, the first of which is implemented, and the procedure is repeated at subsequent steps. By performing constrained optimization, MPC enforces magnitude and rate constraints on the control input as well as constraints on measured outputs to the extent possible based on the current model and unknown disturbances. At step k , PCAC uses the identified model \hat{A}_k , \hat{B}_k , and \hat{C}_k . As in [17], the receding-horizon optimization is performed using quadratic programming (QP), which is a convex optimization technique. This optimization specifies the control input u_{k+1} at the next time step, while also attempting to satisfy constraints on the state and control input

To describe QP-based MPC, let $\mathcal{R}_{k,\ell} \triangleq [r_{k+1}^T \cdots r_{k+\ell}^T]^T \in \mathbb{R}^{\ell p}$ be the vector of future commands over the ℓ -step horizon, let $Y_{1|k,\ell}$ be the corresponding ℓ -step predicted output for a sequence of ℓ future controls, $U_{1|k,\ell}$, and let $Y_{t,1|k,\ell} \triangleq C_{t,\ell} Y_{1|k,\ell}$ be the ℓ -step predicted output, where $C_{t,\ell} \triangleq I_\ell \otimes C_t \in \mathbb{R}^{\ell p_t \times \ell p}$, \otimes is the Kronecker product, and $C_t y_{i|k}$ computes the tracking outputs from $y_{i|k}$. Let $\mathcal{C}_\ell \triangleq I_\ell \otimes (CC_c) \in \mathbb{R}^{\ell n_c \times \ell p}$, where $C_c y_{i|k}$ creates the constrained outputs from $y_{i|k}$, let $\mathcal{D}_\ell \triangleq 1_\ell \otimes \mathcal{D} \in \mathbb{R}^{\ell n_c}$, and define the sequence of differences of control inputs as

$$\Delta U_{1|k,\ell} \triangleq \left[(u_{1|k} - u_k)^T \quad \cdots \quad (u_{\ell|k} - u_{\ell-1|k})^T \right]^T \in \mathbb{R}^{\ell m}. \quad (12)$$

The QP-based MPC optimization problem is then given by

$$\min_{U_{1|k,\ell}} (Y_{t,1|k,\ell} - \mathcal{R}_{k,\ell})^T Q (Y_{t,1|k,\ell} - \mathcal{R}_{k,\ell}) + \Delta U_{1|k,\ell}^T R \Delta U_{1|k,\ell}, \quad (13)$$

subject to

$$C_\ell Y_{1|k,\ell} + \mathcal{D}_\ell \leq 0_{\ell n_c}, \quad (14)$$

$$U_{\min} \leq U_{1|k,\ell} \leq U_{\max}, \quad (15)$$

$$\Delta U_{\min} \leq \Delta U_{1|k,\ell} \leq \Delta U_{\max}, \quad (16)$$

where $Q \triangleq \begin{bmatrix} \bar{Q} & 0_{p_i \times p_i} \\ 0_{p_i \times p_i} & \bar{P} \end{bmatrix} \in \mathbb{R}^{\ell p_i \times \ell p_i}$ is the output weighting, $\bar{Q} \in \mathbb{R}^{(\ell-1)p_i \times (\ell-1)p_i}$ is the cost-to-go output weighting, $\bar{P} \in \mathbb{R}^{p_i \times p_i}$ is the terminal output weighting, $R \in \mathbb{R}^{\ell m \times \ell m}$ is the control-move-size weighting, $U_{\min} \triangleq 1_\ell \otimes u_{\min} \in \mathbb{R}^{\ell m}$, $U_{\max} \triangleq 1_\ell \otimes u_{\max} \in \mathbb{R}^{\ell m}$, $\Delta U_{\min} \triangleq 1_\ell \otimes \Delta u_{\min} \in \mathbb{R}^{\ell m}$, and $\Delta U_{\max} \triangleq 1_\ell \otimes \Delta u_{\max} \in \mathbb{R}^{\ell m}$.

III. Application of PCAC to Boundary-Layer Control

In this section, results are presented for the scenario where PCAC is applied to a supersonic internal flow to control pressure at the sensor location. The geometry utilized in the following studies is a Mach 2.5 inflow internal compression scramjet inlet. While this inlet is not associated with a specific vehicle geometry, it represents a typical geometry for scramjet inlets, and can provide the physical phenomenon of SBLI as observed in a variety of scramjet inlets. The lower surface of the inlet, excluding the bleed port, is set as adiabatic wall boundary condition. The right boundary is an extrapolated boundary condition with first order extrapolation as the flow is supersonic at the outflow, and the left boundary is a fixed inflow. The top boundary is a freestream boundary condition. A schematic of the scramjet inlet with boundary conditions, showing the oblique shock pattern in the inlet and bleed surface location is shown in Figure 3.

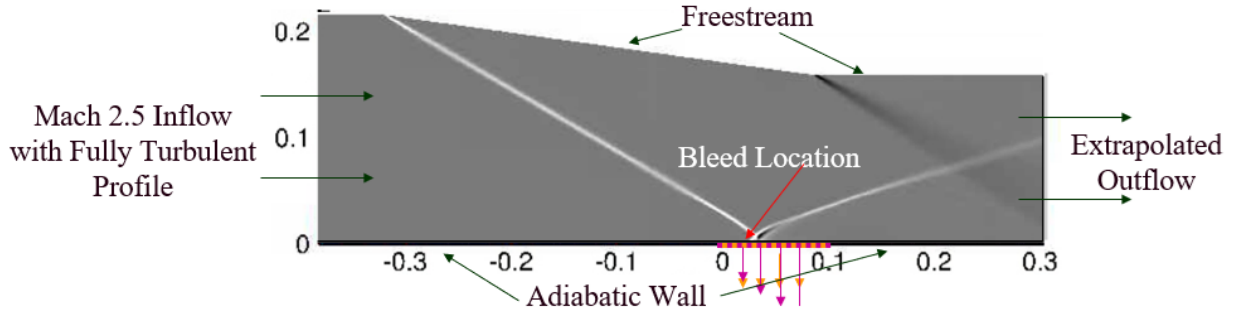


Fig. 3 Schematic of Scramjet Inlet, Boundary Conditions, and Shock Pattern

As mentioned earlier, the flowfield solution was obtained by utilizing Reynolds Averaged Navier Stokes (RANS) with Menter-SST for turbulence closure. Flow enters the domain with a fixed fully turbulent inflow profile and the resulting flowfield includes oblique shocks in the inlet. Integration of VULCAN-CFD and the PCAC control code (CFD-C) was performed with a Linux based code interface written in bash script, which allows for the in-situ information exchange between the computational fluid dynamics (CFD) code and the active control code. The control algorithm uses instantaneous (i.e., every 2 micro-second of physical time) aerothermal variables (e.g., static pressure values at single location on the wall as if a “numerical” sensor is mounted there) as they are calculated by the CFD code. The control code determines the amount of actuation (i.e., bleed-flow rate) required based upon this information, which is transmitted to the CFD via the input file. Then, a new CFD state is calculated based upon the actuation.

The closed-loop CFD simulations consider a pressure command specified at the location of a pressure sensor situated near the wall and bleed port, whose mass-flow rate is specified by PCAC. The “numerical” pressure sensor is placed at the surface next to the location of an oblique shock impinging on the surface, and a rectangular slot bleed port is placed between $x = 0$ and $x = 0.1$ m. An idealized pressure sensor is assumed, which provides a measurement y_k at each time step k . These measurements are used to compute the performance variable z_k , which PCAC uses to specify the next control input u_k . In this case, the static pressure is the measurement and bleed rate is the control input to the CFD simulation. By controlling the local static pressure, boundary-layer thickness is controlled. The numerical examples demonstrate the ability to control the pressure at the sensor location and thus the means for modifying the SBLI and boundary-layer thickness.

Example 1. Low-precision Distributed-Mass-Flux actuator. As mentioned earlier, PCAC is applied to reduce the static pressure at a specified location within the boundary layer by specifying the bleed rate through a bleed-port actuator. In this case, a distributed-mass-flux model was utilized for bleed. Under this model, a perforated plate separates the computational domain from an effusion plenum and the mass flux at each surface cell interface is adjusted based on local flow conditions. A negative mass-flow rate indicates that fluid is flowing out of the computational domain. With this model, the mass-flow rate is distributed over the bleed port and is determined by the local fluid density and temperature. PCAC specifies the mass-flux rate, defined as the mass-flow rate per unit area. The bleed-port actuator is constrained to only allow flow out of the domain, and is precise to the nearest 0.01 kg/m²-s.

Without active control, the static pressure at the sensor location increases to a steady-state static pressure of approximately 17 kPa. Once this steady state is obtained from the CFD solution, PCAC is invoked via the CFD-C interface with static-pressure command of 12 kPa at the sensor location. PCAC begins immediately at step 1, and the static pressure at the sensor location is reduced to the setpoint in 15 steps, where each step is 12 μ s. In physical time, the pressure reduction was achieved in 150 ms. However, the pressure does not converge to the setpoint, and the CFD solution diverges after step 42. It was found that, while the largest mass-flux rate commanded by PCAC was -0.05 kg/m²-s, the mass-flow rate exceeded -1 kg/s, causing the solution to diverge. Figure 4 shows the static-pressure measurements, the control inputs (mass-flux rate), the RLS-estimated model coefficients, and the RLS forgetting factor. Figure 5 shows pressure contours of the flow field at step 1 and 42. At step 42, the pressure decrease near the bleed port is evident along with additional downstream effects.

◇

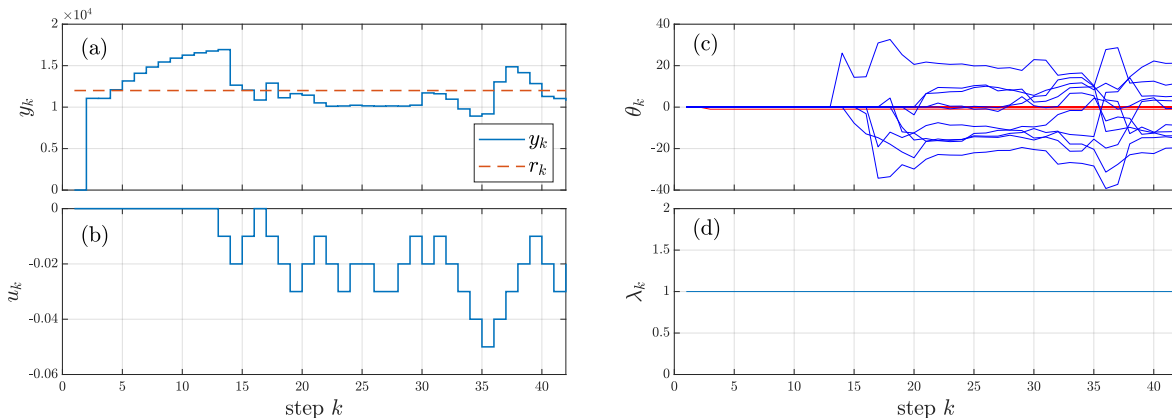


Fig. 4 Example 1: (a) shows that the static pressure at the sensor location is reduced but does not converge to the setpoint. (b) shows the PCAC-commanded bleed mass-flux rate, where negative values indicate flow out of the domain. These values are precise to the nearest 0.01 kg/m²-s. (c) shows the time histories of the numerator (blue) and denominator (red) coefficients of the identified model. (d) shows the variable-rate forgetting factor. Since $\lambda_k \equiv 1$, it follows that forgetting is inactive.

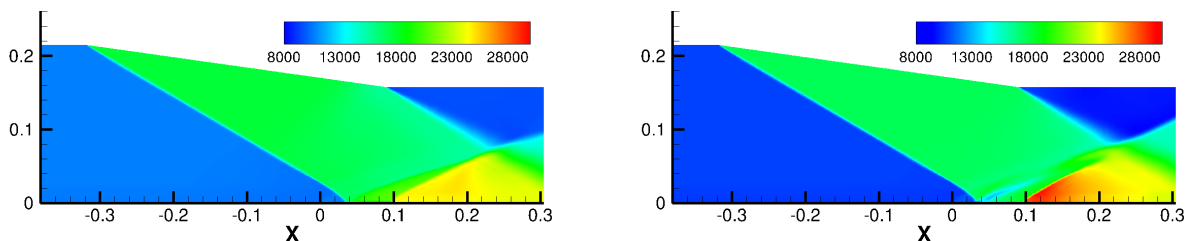


Fig. 5 Example 1: Static pressure contours of the flow at step 1 (left) and step 42 (right). Once the bleed mass flow rate exceeds 1.0 kg/s, the CFD solution diverges.

Example 2. Low-precision Distributed-Mass-Flux actuator. Reconsider Example 1 with a lower static pressure

setpoint of 10 kPa and a modified actuator allowing the bleed mass flux-rate to be specified to the nearest 0.001 kg/m²-s. PCAC begins immediately at step 1 and reduces the pressure in approximately 15 steps, however the oscillations in the requested bleed introduce instability to the CFD, ultimately causing the solution to diverge after 35 steps. This case provides an insight into the maximum allowable bleed mass-flow rate. In this case, the bleed mass-flow rate increased to -1.03 kg/s, resulting in a destabilizing pressure wave in the boundary layer upstream of the bleed port. This caused the CFD solution to diverge.

Figure 6 shows the sensor measurements, the requested control input, the RLS estimated model coefficients, and the RLS forgetting factor. Figure 7 shows pressure contours of the flowfield at steps 1 and 35, where the effect of the oscillating bleed is evident.

◇

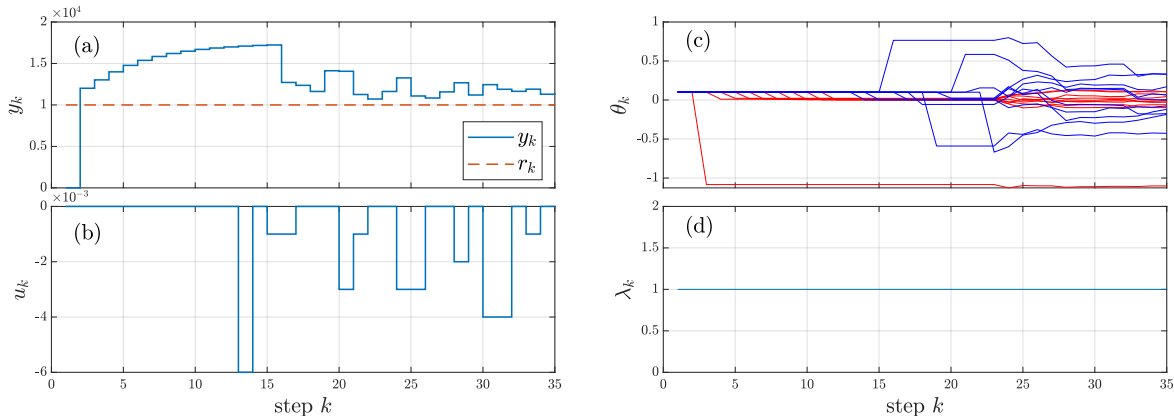


Fig. 6 Example 2: (a) shows that the static pressure at the sensor location is reduced but does not converge to the setpoint. (b) shows the PCAC-commanded bleed mass-flux rate. These values are precise to the nearest 0.001 kg/m²-s. (c) shows the time histories of the numerator (blue) and denominator (red) coefficients of the identified model. (d) shows the variable-rate forgetting factor, which is inactive.

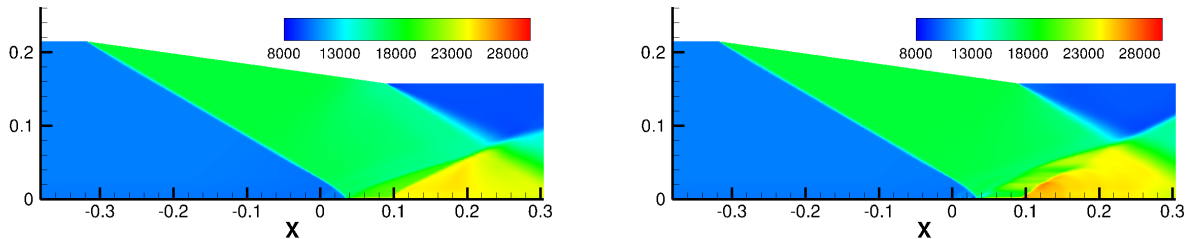


Fig. 7 Example 2: Static pressure contours of the flow at step 1 (left) and step 35 (right). The excessive bleed causes the CFD solver to diverge.

Example 3. Uniform Mass-Flux Bleed Model. Since the distributed mass-flux model did not provide a direct control of mass-flow rate (i.e., the mass flux was specified, which used the local density and temperature values to determine the mass-flow rate) as shown in Examples 1 and 2, an alternative model for bleed mass-flow rate is utilized. This model is called the "uniform mass-flux model," in which the a constant mass-flow rate can be specified over the entire bleed region. A negative mass-flow rate indicates that the fluid is to be effused out of the domain (with the composition and thermal properties of gas in the bleed region).

PCAC begins immediately at step 1 and is able to reduce the measured local pressure near the setpoint pressure in approximately 100 steps (0.12 ms) as shown in Figure 8. The measured pressure approaches the setpoint and is 11.85 kPa at step 266. Oscillations in the requested bleed are present over the first 75 steps as PCAC identifies the system. Despite the oscillations in the requested bleed, the computational solution continues to converge for the duration of the

simulation. Figure 9 shows pressure contours of the flowfield at steps 1 and 266, where the pressure is reduced near the bleed port. In addition, the pressure unsteadiness has reduced, which is an advantage for this application. \diamond

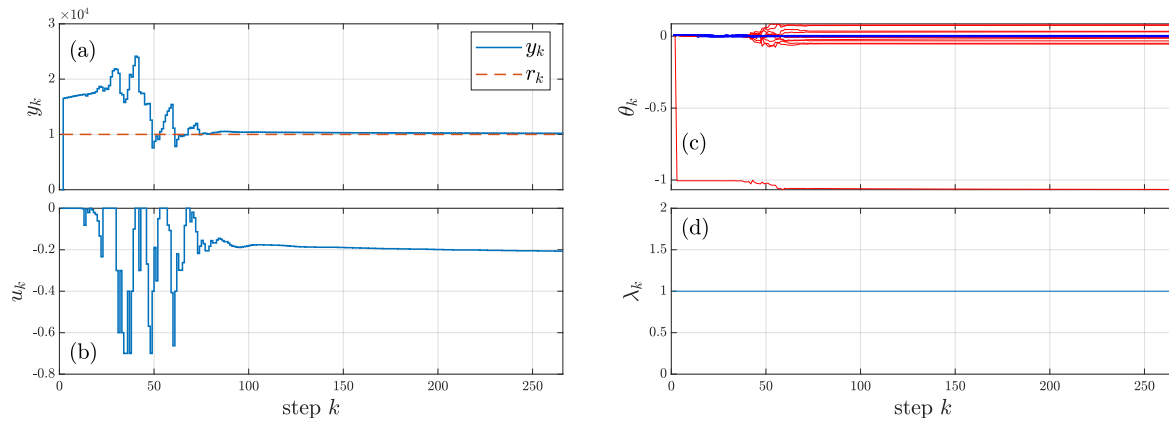


Fig. 8 Example 3: (a) shows that the static pressure at the sensor location approaches the setpoint. (b) shows the PCAC-commanded bleed mass-flow rate, which oscillates over the first 75 steps. These values are precise to the nearest 0.001 kg/s. (c) shows the time histories of the numerator (blue) and denominator (red) coefficients of the identified model. (d) shows the variable-rate forgetting factor, which is inactive.

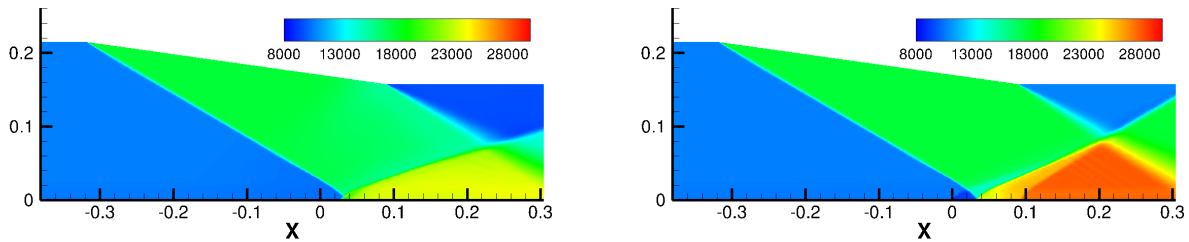


Fig. 9 Example 3: Static pressure contours of the flow at step 1 (left) and step 266 (right).

Example 4. Lower Pressure Setpoint. We repeat Example 3 with the static-pressure setpoint reduced to 7.5 kPa. PCAC begins immediately at step 1 brings the measured static pressure to a slow oscillation around the setpoint in 200 steps, as shown in Figure 10. Figure 11 shows static pressure contours of the flowfield at steps 1 and 250. where the pressure is reduced near the bleed port. Similar to the previous case, the pressure unsteadiness is greatly reduced as a result of bleed. \diamond

Example 5. Higher Pressure Setpoint. In order to further test the ability of the active control methodology, Example 3 is repeated with a higher static-pressure setpoint of 12 kPa. PCAC begins immediately at step 1 and is able to bring the measured static pressure near the setpoint pressure in approximately 200 steps. However, at step 400 the measured pressure remains 283.6 Pa above the setpoint, as shown in Figure 12. The requested bleed and measured pressure continue to have low amplitude oscillations but do not reach a steady state value even after 400 steps. Figure 13 shows pressure contours of the flowfield at steps 1 and 400. \diamond

Example 6. Modified initialization. In this example, we attempt to refine the results in Example 5. Namely, we target the following issues. First issue is that even though the controller is enabled at step 1, no bleed is requested until later steps, thus slowing the response of the system. Second, high-frequency oscillations in the bleed are requested by

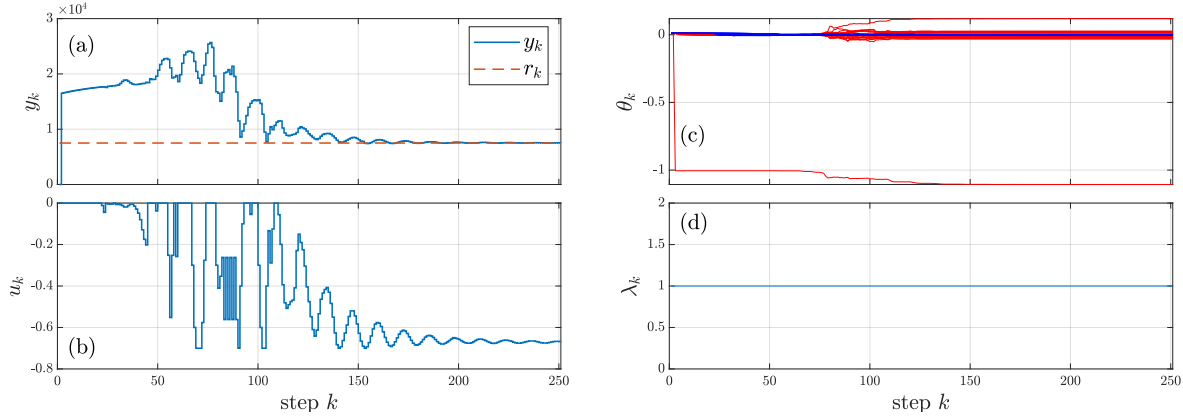


Fig. 10 Example 4: (a) shows that the static pressure at the sensor location is reduced and oscillates around the setpoint. (b) shows the PCAC-commanded bleed mass-flow rate. (c) shows the time histories of the numerator (blue) and denominator (red) coefficients of the identified model. (d) shows the variable-rate forgetting factor, which is inactive.

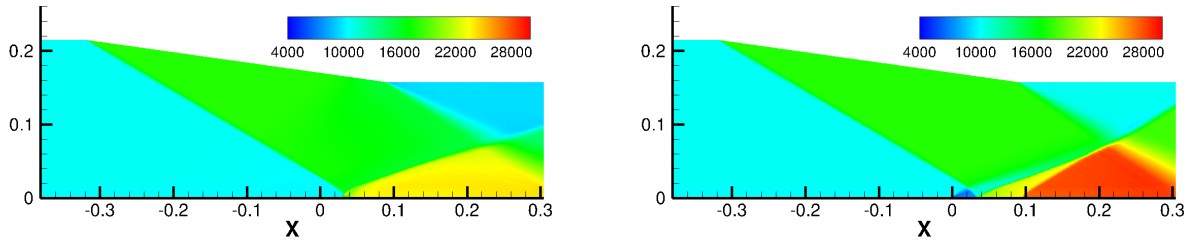


Fig. 11 Example 4: Static-pressure contours of the flow at step 1 (left) and step 250 (right).

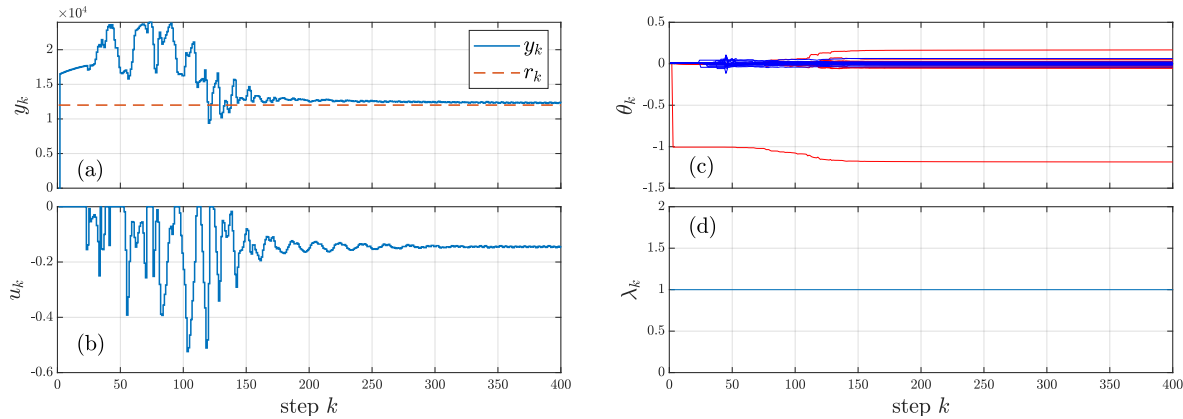


Fig. 12 Example 5: (a) shows that the static pressure at the sensor location is reduced and oscillates above the commanded value. (b) shows the PCAC-commanded bleed mass-flow rate. (c) shows the time histories of the numerator (blue) and denominator (red) coefficients of the identified model. (d) shows the variable-rate forgetting factor, which is inactive.

the controller, and the resulting effects on the flow are undesirable. Third, although the measured pressures are reduced, the pressure does not converge to the setpoint.

Numerical experiments (not shown) indicated that, in the absence of the unilateral constraint on bleed rate, PCAC requested a positive mass-flow rate, which defines flow into the inlet, due to the specified initial system model θ_0 . Since the actuator performs only bleed out of the inlet, the initial control inputs are constrained to 0 kg/s, and remain at 0

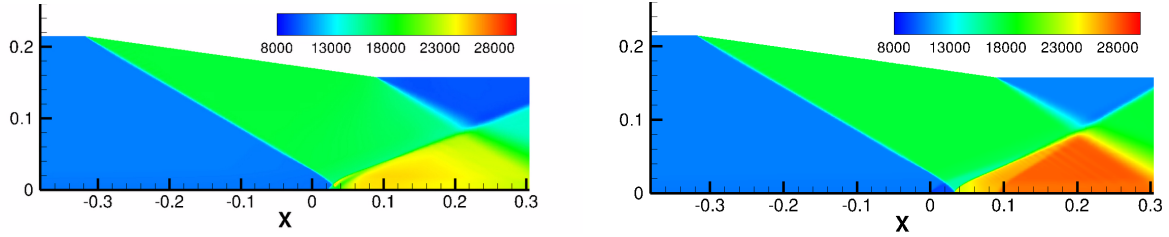


Fig. 13 Example 5: Static pressure contours of the flow at step 1 (left) and step 400 (right).

kg/s until the identified model is updated. When the requested bleed is 0 kg/s, the identified model is slowly updated by noise in the solution and by other system dynamics not involving the bleed actuation. These dynamics require an unpredictable number of steps to update the model sufficiently to allow a nonzero bleed to be requested. This issue was resolved by selecting an initial system model θ_0 that resulted in an initial requested bleed-rate consistent with the unilateral constraint.

In Figure 14, the controller is enabled at step 10. Immediately at step 10, the controller requests a nonzero bleed rate. Additional adjustments are made to the controller hyperparameters to bring the measured pressure to an oscillation around the setpoint. However, the oscillations have larger amplitude than in Example 5.

◇

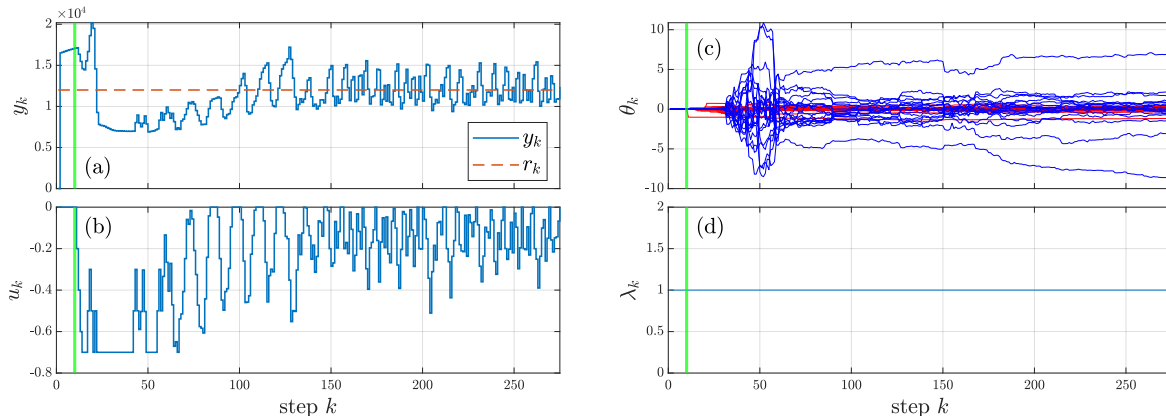


Fig. 14 Example 6: (a) shows that the static pressure at the sensor location is reduced but does not converge to the commanded value. (b) shows the PCAC-commanded bleed mass-flow rate, which is nonzero as soon as the controller is enabled at step 10 (indicated by the green line). (c) shows the time histories of the numerator (blue) and denominator (red) coefficients of the identified model. (d) shows the variable-rate forgetting factor, which is inactive.

Example 7. Open-loop Bleed. Motivated by the inability to reduce the oscillations in the measured pressure and to reduce the error between the measured and setpoint pressures, the time-varying effect of the bleed on the pressure at the sensor location was studied. First, a harmonic bleed mass-flow rate is prescribed, where the bleed rate cycles between 0 and 0.7 kg/s as shown in Figure 15. After the initial transient response, the measured pressure exhibits a nonlinear response. Specifically, the measured pressure increases rapidly once it rises above about 11 kPa and decreases slowly after it falls below about 11 kPa. While this simulation does not use closed-loop feedback control, RLS is still used to identify a system model. Figure 15 shows that the identified model coefficients do not converge, which indicates poor system identification. The poor identification hinders system performance, particularly when the setpoint pressure is near 11 kPa.

In Figure 16, a harmonic bleed is applied with reduced amplitude and bias such that the measured pressure remains below 11 kPa. The response in pressure in this region appears harmonic, indicating that the response is approximately linear over this range of bleed rates and measured pressures. As shown in, Figure 16, the resulting system identification

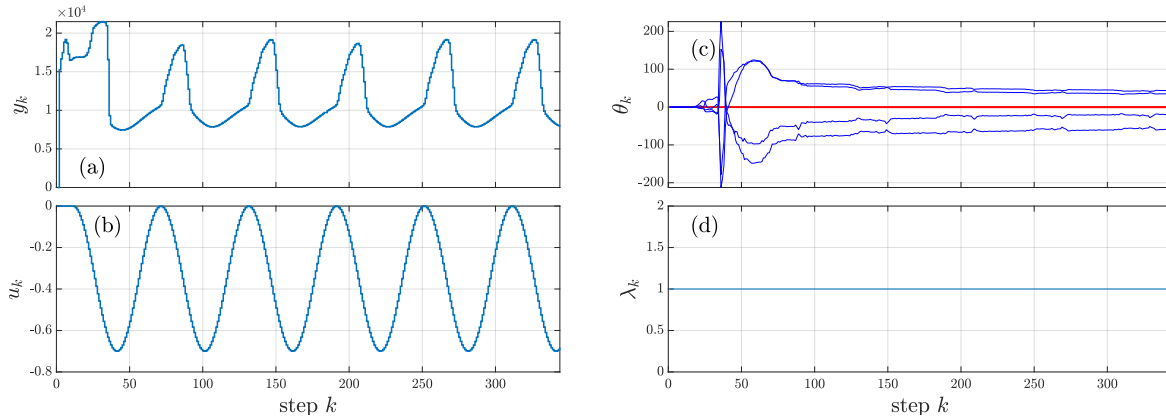


Fig. 15 Example 7: (a) shows the resulting effect on pressure at the sensor location due to the harmonic bleed shown in (b). A sudden change in the rate of pressure change occurs near 11 kPa. While the controller is not specifying the control inputs in a closed loop, identification is active and (c) shows that the identified model does not converge.

converges, indicating a more accurate system identification.

◇

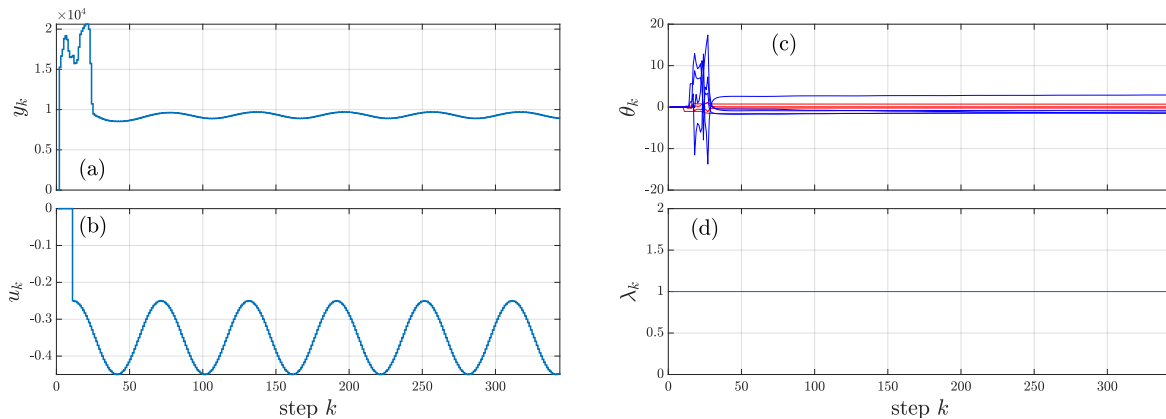


Fig. 16 Example 7: (a) shows the resulting effect on pressure at the sensor location due to the harmonic bleed shown in (b), where the bleed is prescribed to keep the pressure below 11 kPa. While the controller is not specifying the control inputs in closed loop, identification is active, and (c) shows that the identified model converges.

Example 8. Pressure Setpoint in Linear Region. Motivated by the findings in Example 7, and with the improvement in the controller initialization from Example 6, a pressure setpoint of 9 kPa, which is in the approximately linear region of pressures found in Example 7, is specified. Figure 17 shows that the controller requests nonzero bleed immediately once it is enabled and that the measured pressure approaches the pressure setpoint with an oscillation that damps out. The amplitude of the oscillations are reduced from those in Example 5 and have a smaller effect on the measured pressure. The measured pressure approaches the pressure setpoint and is 9.62 kPa at step 400. Figure 20 shows pressure contours of the flowfield where the pressure is reduced near the bleed port.

While the pressure setpoint is in the approximately linear range, the controller must bring the pressure through the nonlinear range to converge to the pressure setpoint, which may have an adverse effect on the system identification. To avoid this, the example was repeated by prescribing 0.7 kg/s of bleed mass-flow rate for the 10 steps before the controller was enabled. As soon as the controller was enabled, PCAC specified the requested bleed rate. Figure 19 shows that, by prescribing this initial bleed, the controller began its ID with the pressure in the approximately linear region, and the

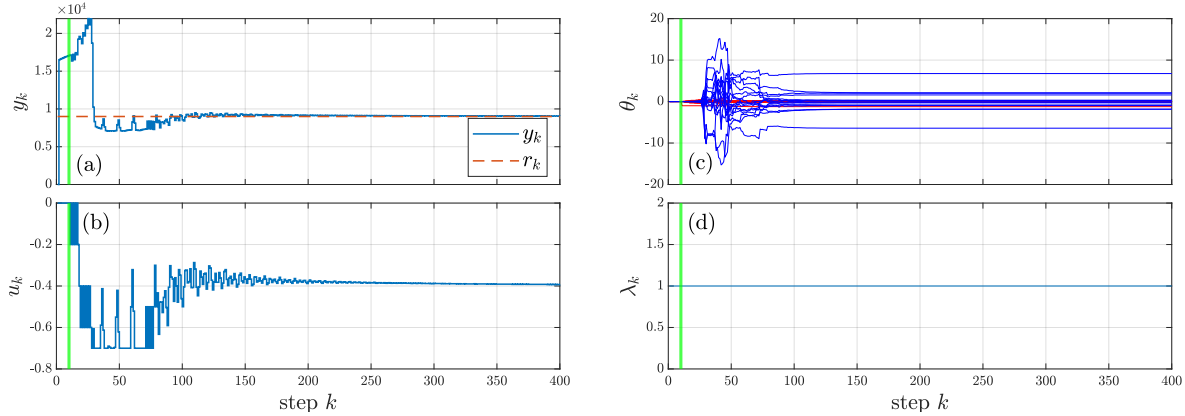


Fig. 17 Example 8: With a bleed mass-flow rate of 0 kg/s over the first 10 steps, (a) shows that the static pressure approaches the setpoint. (b) shows the PCAC-commanded bleed mass-flow rate. (c) shows the time histories of the numerator (blue) and denominator (red) coefficients of the identified model. (d) shows the variable-rate forgetting factor, which is inactive.

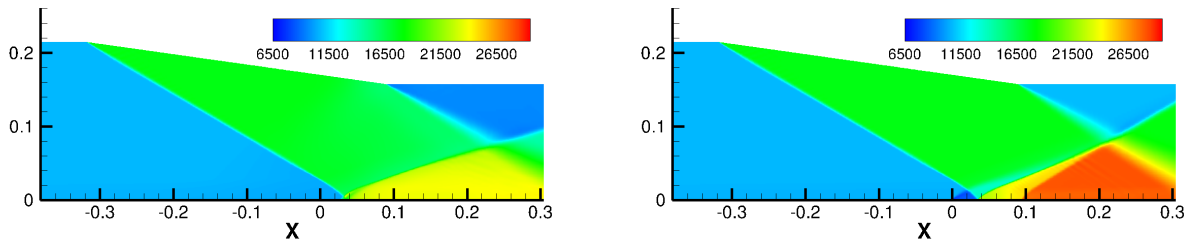


Fig. 18 Example 8: Static pressure contours of the flow at step 1 (left) and step 400 (right).

resulting system response showed low amplitude oscillations. The measured pressure approached the setpoint, and the error between the measured pressure and the setpoint at step 400 is 8 Pa, which is a very small value with respect to the target static pressure. Figure 20 shows pressure contours of the flowfield where the pressure is reduced near the bleed port. \diamond

IV. Conclusions

This paper presented results on active flow control using predictive cost adaptive control (PCAC) working in-situ with supersonic inlet flow-physics via an interface developed under this research. It was found that PCAC can control the boundary-layer separation phenomenon, which is a known instability mechanism with the potential to begin inlet unstart. In-situ active control of a scramjet with an optimized sensor and actuator placement based upon the scramjet flow physics will have numerous benefits including the ability to fly aggressive trajectories, achieve larger ranges with reduced takeoff weights, and increase payload weights. Future work will involve the study of changing conditions including incoming flow velocity and angle of attack. Additionally, the effectiveness of PCAC with the inclusion of integral action and of PCAC with a nonlinear identification scheme will be considered.

V. Acknowledgments

The authors would like to acknowledge the support from Office of Naval Research and Dr. Eric Marineau via grant number N00014-22-1-2457.

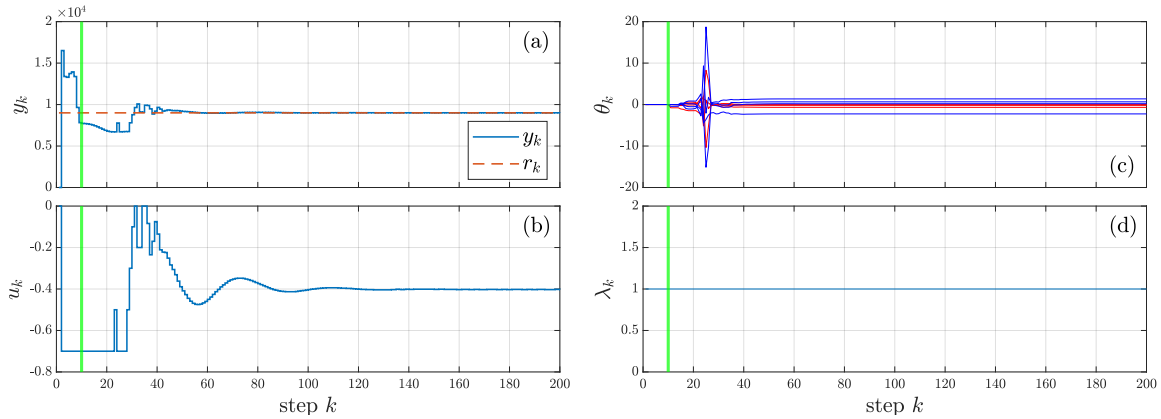


Fig. 19 Example 8: With a bleed mass-flow rate of -0.7 kg/s over the first 10 steps, (a) shows that the static pressure at the sensor location approaches the setpoint with lower oscillations (b) shows the PCAC-commanded bleed mass-flow rate which is smooth compared to previous examples. (c) shows the time histories of the numerator (blue) and denominator (red) coefficients of the identified model. (d) shows the variable-rate forgetting factor, which is inactive.

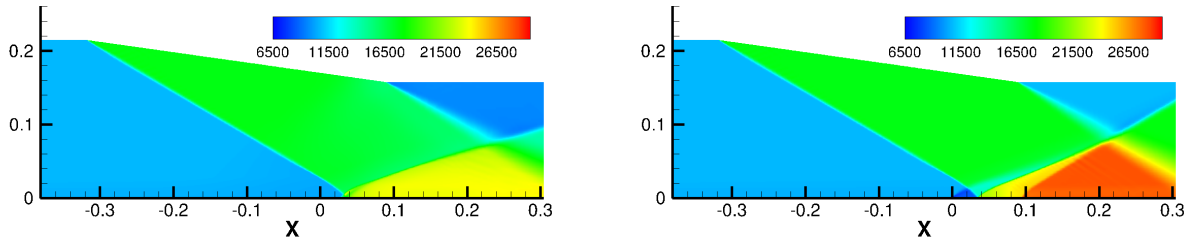


Fig. 20 Example 8: Static pressure contours of the flow at step 1 (left) and step 200 (right).

References

- [1] Heiser, W., Pratt, D., Daley, D., and Mehta, U., *Hypersonic Airbreathing Propulsion*, AIAA, 1994. <https://doi.org/10.2514/4.470356>.
- [2] Curran, E. T., "Scramjet Engines: The First Forty Years," *J. Propulsion and Power*, Vol. 17, No. 6, 2001, pp. 1138–1148. <https://doi.org/10.2514/2.5875>.
- [3] Waltrup, P., Gravlin, E., White, M., and Zarlingo, F., "History of U.S. Navy Ramjet, Scramjet, and Mixed-Cycle Propulsion Development," *J. Propulsion and Power*, Vol. 18, 2002, pp. 14–27. [10.2514/2.5928](https://doi.org/10.2514/2.5928).
- [4] Fry, R. S., "A Century of Ramjet Propulsion Technology Evolution," *J. Propulsion and Power*, Vol. 20, No. 1, 2004, pp. 27–58. <https://doi.org/10.2514/1.9178>.
- [5] Morgan, B., Duraisamy, K., and Lele, S. K., "Large-eddy simulations of a normal shock train in a constant-area isolator," *AIAA Journal*, Vol. 52, No. 3, 2014, p. 539–558. <https://doi.org/10.2514/1.j052348>.
- [6] Acharya, R., Palies, P., Schetz, J., and Schmisser, J., "Development of Uncertainty Quantification Framework Applied to Scramjet Unstart Challenge," *AIAA Paper*, March 2020. <https://doi.org/10.2514/6.2020-2434>.
- [7] Sethuraman, V. R. P., Kim, T. H., and Kim, H. D., "Control of the oscillations of shock train using boundary layer suction," *Aerospace Science and Technology*, Vol. 118, No. 107012, 2021, pp. 1872, 1873. <https://doi.org/10.1016/j.ast.2021.107012>.
- [8] Islam, S. A. U., and Bernstein, D. S., "Recursive Least Squares for Real-Time Implementation," *IEEE Contr. Syst. Mag.*, Vol. 39, No. 3, 2019, pp. 82–85.
- [9] Bruce, A. L., Goel, A., and Bernstein, D. S., "Convergence and consistency of recursive least squares with variable-rate forgetting," *Automatica*, Vol. 119, 2020, p. 109052.

- [10] Goel, A., Bruce, A. L., and Bernstein, D. S., “Recursive Least Squares With Variable-Direction Forgetting: Compensating for the Loss of Persistency [Lecture Notes],” *IEEE Control Systems Magazine*, Vol. 40, No. 4, 2020, pp. 80–102.
- [11] Bruce, A. L., Goel, A., and Bernstein, D. S., “Necessary and Sufficient Regressor Conditions for the Global Asymptotic Stability of Recursive Least Squares,” *Sys. Contr. Lett.*, Vol. 157, 2021, pp. 1–7. Article 105005.
- [12] Mohseni, N., and Bernstein, D. S., “Recursive least squares with variable-rate forgetting based on the F-test,” *Proc. Amer. Contr. Conf.*, 2022, pp. 3937–3942.
- [13] Polderman, J. W., “A State Space Approach to the Problem of Adaptive Pole Assignment,” *Mathematics of Control, Signals and Systems*, Vol. 2, No. 1, 1989, pp. 71–94.
- [14] “VULCAN, <http://vulcan-cfd.larc.nasa.gov/>,” 2017.
- [15] Mohseni, N., and Bernstein, D. S., “Recursive Least Squares with Variable-Rate Forgetting Based on the F-Test,” *Proc. Amer. Contr. Conf.*, 2022, pp. 3937–3942.
- [16] McKeon, J. J., “F approximations to the distribution of Hotelling’s T_0^2 ,” *Biometrika*, Vol. 61, No. 2, 1974, pp. 381–383.
- [17] Nguyen, T. W., Islam, S. A. U., Bernstein, D. S., and Kolmanovsky, I. V., “Predictive Cost Adaptive Control: A Numerical Investigation of Persistency, Consistency, and Exigency,” *IEEE Contr. Sys. Mag.*, Vol. 41, 2021, pp. 64–96.